Modeling complex geological structures with elementary training images and transform-invariant distances

Gregoire Mariethoz[1] and Bryce F. J. Kelly[1]

Received 14 January 2011; revised 21 April 2011; accepted 20 May 2011; published 14 July 2011.

[1] We present a new framework for multiple-point simulation involving small and simple training images. The use of transform-invariant distances (by applying random transformations) expands the range of structures available in the simple patterns of the training image. The training image is no longer regarded as a global conceptual geological model, but rather a basic structural element of the subsurface. Complex geological structures are obtained whose spatial structure can be parameterized by adjusting the statistics of the random transformations, on the basis of field data or geological context. In most cases, such parameterization is possible by adjusting two numbers only. This method allows us to build models that (1) reproduce shapes corresponding to a desired prior geological concept and (2) are in phase with different types of field observations such as orientation, hydrofacies, or geophysical measurements. The main advantage is that the training images are so simple that they can be easily built even in 3-D. We apply the method on a synthetic example involving seismic data where the transformation parameters are data-driven. We also show examples where realistic 2- and 3-D structures are built from simplistic training images, with transformation parameters inferred using a small number of orientation data.

Citation: Mariethoz, G., and B. F. J. Kelly (2011), Modeling complex geological structures with elementary training images and transform-invariant distances, *Water Resour. Res., 47*, W07527, doi:10.1029/2011WR010412.

1. Introduction

[2] Numerical subsurface models often rely on scarce data that are insufficient for determining the nature of the geological continuity at a given site. Hence, in most situations the geologist's contextual insights are a crucial source of prior information. In the Earth sciences, a prior model represents this knowledge, i.e., what is known of the geological continuity before the inclusion of location-dependent data. In general, the fewer local data available, the greater the importance of the prior model. Prior spatial continuity can be characterized in various ways. Figure 1 illustrates various prior concepts of geological continuity that can have very different implications in terms of flow and transport properties. They could, for example, correspond to: (1) folded parallel structures of alternating high and low permeability values (Figure 1a and 1b); (2) high permeability values well connected together and defining boundaries between disconnected blocks of low values (Figure 1c and 1d); (3) low permeability values well connected together and defining boundaries between disconnected blocks of high values (Figure 1e); and (4) connectivity of high values and connectivity of low values, spatially arranged as elongated bodies (Figure 1f).

[3] Existing geostatistical simulation methods are able to represent such priors. However, at present only multi-Gaussian models offer the possibility to easily define the spatial structure with only a few parameters (mean, variance, and correlation length). Therefore, the multi-Gaussian framework offers possibilities for including such parameters in optimization frameworks [*Kitanidis*, 1995; *Nowak et al.*, 2010], e.g., finding the variogram parameters that are coherent with state data such as groundwater head or concentration measurements.

[4] Within the multi-Gaussian framework, a wealth of techniques exist to generate diverse shapes by combining different Gaussian random fields, such as the plurigaussian method [*Le Loc'h and Galli*, 1994; *Mariethoz et al.*, 2009] or the random coordinate perturbation method and the random mixture of Gaussian fields [*Emery*, 2007]. These methods have the advantage of allowing for parameterization of the prior through the definition of correlation ranges, cutoffs, etc. A parametric spatial model is of interest for model inference and inverse modeling. In certain cases, however, the assumptions underlying these multi-Gaussian models do not allow for the reproduction of the behavior of highly heterogeneous aquifers, especially when connectivity patterns play an important role [*Bastante et al.*, 2008; *Gómez-Hernández and Wen*, 1998; *Knudby and Carrera*, 2005; *Sánchez-Vila et al.*, 1996; *Western et al.*, 2001]. This can have an especially strong impact when modeling transport processes [*Green et al.*, 2010; *Klise et al.*, 2009; *Zinn and Harvey*, 2003]. Therefore, several alternative simulation methods have been developed in the past decades. One approach is to use parametric mathematical models,

[1]National Centre for Groundwater Research and Training, University of New South Wales, Sydney, New South Wales, Australia.

0043-1397/11/2011WR010412

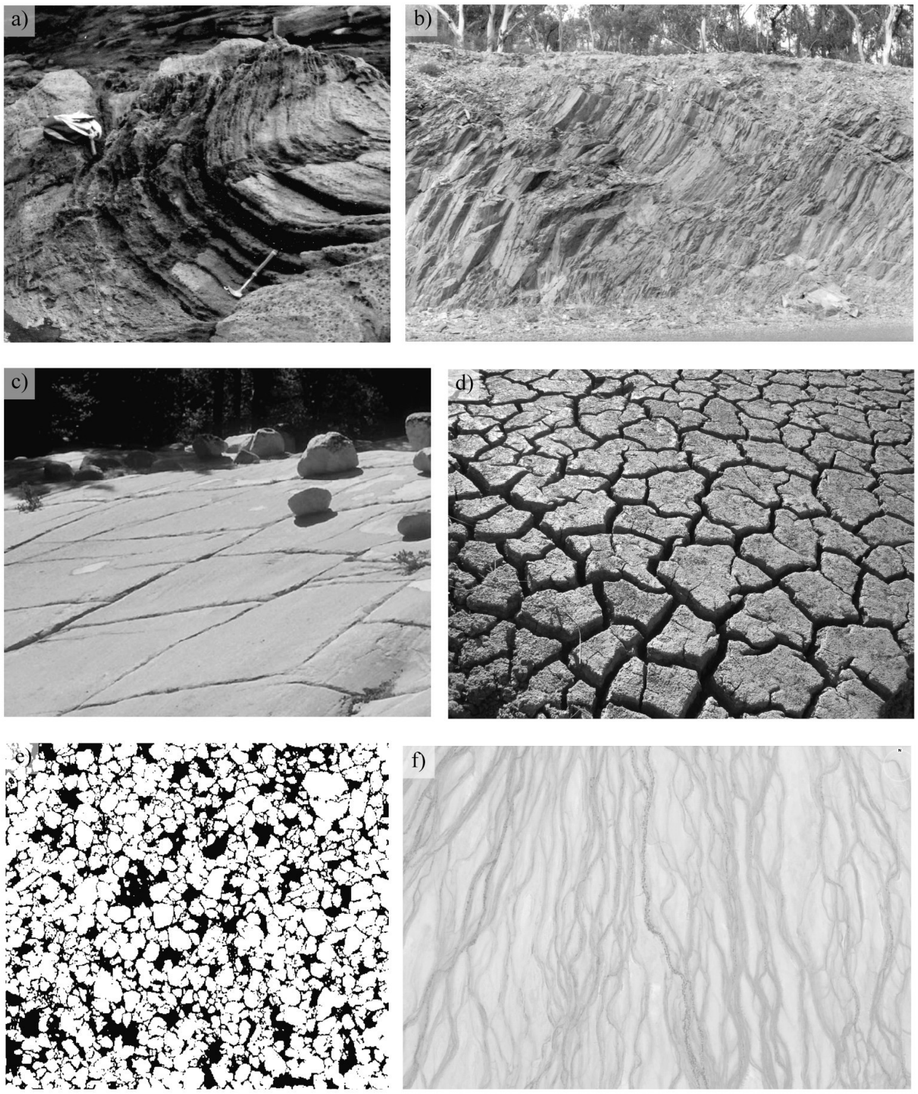

Figure 1. Different prior concepts of geological continuity. (a) Slump folding in mudstone, Warden Head, New South Wales, Australia. (b) Kink folds in interbedded phyllite and quartz greywacke, Kelso-Sofala Road, New South Wales, Australia. (c) Jointed granite, Sierra Mountain, California, United States. (d) Desiccation cracks in Vertosol soil, Narrabri, New South Wales, Australia. (e) Hawkesbury Sandstone thin section. (f) Braided river channels, Diamantina River, Queensland, Australia (image Google Earth, Cnes/Spot, Whereis Sensis, DigitalGlobe). (Figures 1a–1c and Figure 1e courtesy of Bryce Kelly. Figure 1d courtesy of Anna Greve.)

but to enrich the statistical information by including high-order measures of spatial continuity. Among this promising class of methods spatial cumulants [*Dimitrakopoulos et al.*, 2010] and copulas [*Bárdossy and Li*, 2008] have recently received a lot of attention.

[5] Other approaches such as object-based [e.g., *Deutsch and Wang*, 1996; *Deutsch and Tran*, 2002; *Keogh et al.*, 2007; *Pyrcz et al.*, 2009] and pseudo-genetic models [*Cojan et al.*, 2004; *Michael et al.*, 2010] have been traditionally used to account for the existence of specific connectivity patterns. The main advantage is their ability to define basic shapes that represent geological bodies, using physical representations of the primary geological processes and settings. Conditioning to points data and to nonstationarity in the objects' proportions can be accomplished through a birth and death algorithm [*Allard et al.*, 2006; *Lantuéjoul*, 2002], but technical and computational difficulties remain when large amounts of data are present. One of the advantages of the Boolean framework is that the characteristics of the objects used in the simulation can be adjusted to a certain extent (e.g., channel width, sinuosity, etc.).

[6] Recent advances in the domain of geostatistical simulations include multiple-point simulation methods (MPS), which use prior spatial models given by nonparametric conceptual example images, namely training images. The principle of a training image is appealing to geologists because it is a direct representation of a geological concept [*Feyen and Caers*, 2006]. It has been shown that MPS are able to produce geologically realistic structures by using high-order spatial statistics, which can represent a wide

range of spatially structured, low entropy phenomena, and have been used in a variety of cases [e.g., *Caers*, 2003; *Gonzales et al.*, 2008; *Hu and Chugunova*, 2008; *Huysmans and Dassargues*, 2009; *Journel and Zhang*, 2006; *Lu et al.*, 2009; *Okabe and Blunt*, 2007; *Ronayne et al.*, 2008; *Wojcik et al.*, 2009; *Wu et al.*, 2008].

[7] However, although MPS has in recent years become an invaluable tool to integrate geological concepts in subsurface models, the method is still difficult to apply in cases when one does not have enough information to clearly decide which training image to use [*de Almeida*, 2010; *Pyrcz et al.*, 2008]. Even when the geological context is clear, it is a lengthy geomodeling exercise to build a complex 3-D training image that adequately represents the complexity of geological structures.

[8] Another difficulty is related to the parameterization of the training image. Since the choice of a training image is a discrete decision (either image A or B), it is not straightforward to parameterize it. *Suzuki and Caers* [2008] proposed a methodology for investigating prior uncertainty in the context of inverse problems through the use of distances between a large variety of discrete scenarios. However, it is still highly desirable to parameterize different multiple-point priors with only a few continuous parameters, in a similar way as multi-Gaussian priors. This is generally not possible because the training images normally used are too complex to be parameterized simply. Training images are generally large (*Strebelle* [2002] recommends use of a training image much larger than the simulation domain) and ideally contain enough diversity to encompass all possible patterns to be found in the simulation domain.

[9] Even if robust tools exist for multiple-point simulation, the practical difficulties related to building and parameterizing the training image often lead to discarding multiple-point methods and to adopt parametric alternatives for the inferences of spatial continuity, such as traditional variogram-based techniques. Nonetheless, there are cases where more prior information is available than a two-point model of spatial correlation. For example, on a given site, one can often determine very general prior characteristics (e.g., connectivity or disconnectivity of the high values), but the precise types of structures (orientation and dimensions of the structures) are usually uncertain. In these cases, it is desirable to have methods that integrate such prior characteristics in stochastic models while leaving unknown characteristics random.

[10] In this paper we present a new concept and algorithm for multiple-point simulation that considers elementary/simplistic training images that are an expression of prior spatial continuity. During the simulation the diversity of patterns is enriched by applying random transformations. It is equivalent to comparing patterns up to a transformation, or using a transform-invariant distance. This method enables the generation of complex geological images whose spatial structure can be parameterized by adjusting the statistics of the random transformations. In most cases, such parameterization is possible by adjusting only two numbers. It allows parameterizing multiple-point priors in a straightforward and integrated manner. Moreover, it also resolves the problem of building a training image because building elementary images is easy even in 3-D. The training image is no longer regarded as a global conceptual geological model, but rather a basic structural element of the subsurface, such as the shapes used in object-based simulations. These basic elements can be parameterized to create models that (1) reproduce shapes corresponding to a desired prior geological concept, and (2) are in phase with different types of field observations such as orientation, hydrofacies, or geophysical measurements.

[11] Section 2 of the paper is a short description of the direct sampling method, which is the geostatistical simulation method used to illustrate our concept. Note, however, that the fundamental idea could, in theory and regardless of implementation issues, be applied to any simulation algorithm that is based on the computation of a distance between patterns. Section 3 details the concept of transform-invariant distances and elementary training images, and illustrates this concept with basic examples. Section 4 shows how conditioning data can be used to structurally guide the simulation. Finally, Section 5 shows how to introduce nonstationarity in the transformation parameters to model complex geological structures.

2. Background on the Direct Sampling Method

[12] The direct sampling method is described in details in the work of *Mariethoz et al.* [2010] as a multiple-point simulation tool, although it was found that a similar algorithm had been proposed a decade earlier by *Erfos and Leung* [1999] in the context of texture synthesis. It generates conditional multiple-point simulations that present the same spatial dependence as a user-defined training image. Note that we use the term spatial dependence and not spatial correlation to emphasize that no linearity is assumed. Direct sampling is a sequential simulation method. It proceeds by successively visiting all locations $\mathbf{x}$ of a regular grid, each time assigning a value $Z(\mathbf{x})$ that depends on the values of the neighboring locations of $\mathbf{x}$, denoted $Z(\mathbf{x}_1)$, $Z(\mathbf{x}_2)$, ... $Z(\mathbf{x}_n)$, and on the lag vectors defining the position of each neighbor relative to $\mathbf{x}$, denoted $\mathbf{h}_1$, $\mathbf{h}_2$, ..., $\mathbf{h}_n$. For simplicity, we denote $\mathbf{N}_x$ the neighborhood of $\mathbf{x}$, comprising both the lag vectors and the values at the neighboring locations. Figure 2 illustrates the different components of $\mathbf{N}_x$.

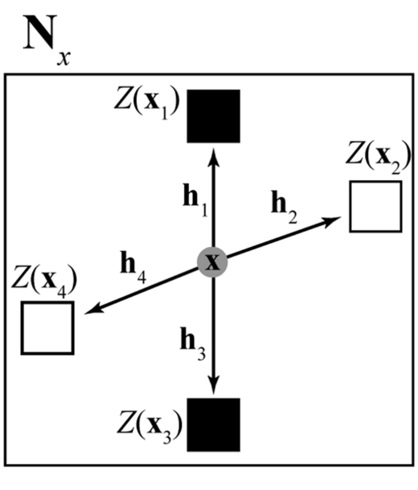

Figure 2. The different elements defining N_x, the neighborhood of the location x.

[13] The direct sampling algorithm is summarized below:

Input: (1) Simulation grid SG with locations denoted **x**, (2) training image TI with locations denoted **y**, (3) distance function *d*(.) bounded in [0,1], (4) distance threshold *t* (distance under which two neighborhoods are considered identical).

1. **While** # noninformed locations in SG ≥ 0 **do**.
2. Choose a noninformed location **x** in SG and identify the neighborhood $\mathbf{N}_x$ centered on **x**.
3. Initialize $d(\mathbf{N}_x, \mathbf{N}_y) = \infty$.
4. **While** $d(\mathbf{N}_x, \mathbf{N}_y) \geq t$ **do**.
5. Sample a location **y** in TI.
6. Define $\mathbf{N}_y$ as the neighborhood centered on **y** having identical lag vectors as $\mathbf{N}_x$.
7. Compute the distance $d(\mathbf{N}_x, \mathbf{N}_y)$.
8. **End While**.
9. Assign $Z(\mathbf{x}) = Z(\mathbf{y})$.
10. **End While**.

Output: Completed simulation SG.

The main principle is that as soon as a matching neighborhood is found (i.e., when $d(\mathbf{N}_x, \mathbf{N}_y) < t$, one can consider that ($\mathbf{N}_y \equiv \mathbf{N}_x$), the corresponding value $Z(\mathbf{y})$ is a sample of the conditional distribution Prob $\{Z(\mathbf{x})|\mathbf{N}_x\}$).

[14] The distance $d(\mathbf{N}_x, \mathbf{N}_y)$ can be computed in different ways depending on the nature of the variable *Z*. It was shown by *Mariethoz et al.* [2010] that choosing the appropriate distance allows one to adapt the method to either categorical or continuous variable cases, and also to jointly simulate several dependant variables. The distances proposed include, for a categorical variable,

$$d(\mathbf{N}_x, \mathbf{N}_y) = \frac{1}{n}\sum_{i=1}^{n} a_i \quad \in [0,1], \qquad \text{where } a_i = \begin{cases} 0 & \textit{if } Z(\mathbf{x}_i) = Z(\mathbf{y}_i) \\ 1 & \textit{if } Z(\mathbf{x}_i) \neq Z(\mathbf{y}_i) \end{cases}, \tag{1}$$

and for a continuous variable, the normalized Manhattan distance

$$d(\mathbf{N}_x, \mathbf{N}_y) = \frac{1}{n}\sum_{i=1}^{n} \frac{|Z(\mathbf{x}_i) - Z(\mathbf{y}_i)|}{\max_{y \in TI} Z(y) - \min_{y \in TI} Z(y)}. \tag{2}$$

[15] Since the distances are usually defined such that they are within the interval [0,1], the threshold is also bound to the same interval. Defining a threshold of $t = 0$ means that the patterns of the training image will be reproduced with the highest possible accuracy. Conversely, when setting $t = 1$, the algorithm unconditionally samples values from the training image, therefore reproducing the marginal distribution of *Z* but with no spatial dependence. Between these two extreme cases, the value of *t* determines how accurately the patterns of the training image are reproduced.

3. Transform-Invariant Distances

3.1. The Principle of Transform-Invariant Distances

[16] Let us define a geometrical transformation T_p applied to $\mathbf{N}_x$, where *p* is a parameter affecting the transformation. Several types of geometrical transformations can be considered. For now, we consider two types of transformations, which are (1) rotations centered on **x**, denoted *R*(.), and (2) affinity (or homothetic) transforms, denoted *A*(.). Note that we consider only geometrical transforms that affect the lag vectors **h** while the values $Z(\mathbf{x}_i)$ remain unchanged. For rotations, the parameter *p* corresponds to the rotation angle and for affinity transforms, it corresponds to the affinity ratio. Figure 3 shows a few examples of transformations applied to a simple neighborhood (or pattern) $\mathbf{N}_x$.

[17] The direct sampling method uses a distance between a neighborhood $\mathbf{N}_x$ centered on the location **x**, and another neighborhood $\mathbf{N}_y$ centered on location **y** in the training image (see step 7 of the algorithm). Instead, we propose a consideration of the distance between the ensemble of possible neighborhoods resulting from geometric transforms of $\mathbf{N}_x$ and a neighborhood $\mathbf{N}_y$ in the training image. By doing this, we compare the neighborhoods $\mathbf{N}_x$ and $\mathbf{N}_y$ *up to a transformation* (i.e., there exists a transformation *T*(.) that makes $T(\mathbf{N}_x)$ identical to $\mathbf{N}_y$). When considering transform-invariant distances, Figure 3a, 3b, and 3c are identical up to a rotation, and Figure 3a, 3d, and 3e are identical up to an affinity. We define a transform-invariant distance as

$$d^T(\mathbf{N}_x, \mathbf{N}_y) = \operatorname{argmin}\{d[T_p(\mathbf{N}_x), \mathbf{N}_y]\} : \forall p \text{ in } [a,b], \tag{3}$$

where *a* and *b* are bounds specified for parameter *p*. A transform-invariant distance can be computed by finding a value of *p* (in the interval [*a,b*]) such that the distance $d[T_p(\mathbf{N}_x), \mathbf{N}_y]$ is minimal. Once the value of *p* is found, the corresponding distance is the transform-invariant distance. Note that the parameter *p* is not prescribed in advance, but determined by a search procedure that evaluates all *p* values in [*a,b*] and finds one corresponding to an acceptable distance (or mismatch) between both neighborhoods.

[18] Since the direct sampling method only needs to sample a single neighborhood $\mathbf{N}_y$ whose distance to $\mathbf{N}_x$ is lower than the threshold *t*, using a transform-invariant distance simply consists of applying to $\mathbf{N}_x$ a transformation with a random *p*-value in [*a,b*] each time the distance $d(\mathbf{N}_x, \mathbf{N}_y)$ is computed. This is accomplished by applying the random transformation at step 7 of the direct sampling algorithm presented in Section 2. As soon as $d[T_p(\mathbf{N}_x), \mathbf{N}_y] \leq t$, one can consider that $\mathbf{N}_y \equiv \mathbf{N}_x$ (up to a transformation T_p) and assign $Z(\mathbf{x}) = Z(\mathbf{y})$. This sampling procedure is equivalent to searching the entire interval [*a,b*], but much less computationally demanding.

[19] When using transform-invariant distances in multiple-point simulations, one does not only consider the patterns found in the training image, but all their possible transformations in the range [*a,b*]. This extra degree of freedom constitutes a considerable increase in the diversity of the possible structures that can be produced, and allows complex spatial patterns to be generated, even from simple training images. By adjusting the values of the transformation parameter bounds (either constant or spatially variable), it is possible to parameterize the ensemble of patterns available for the simulation. The consequence is a controlled increase in the variability between realizations. *Emery and Ortiz* [2011] recently showed that a robust use of a complex training image would call for a dramatic increase in the training image size, to the point that it

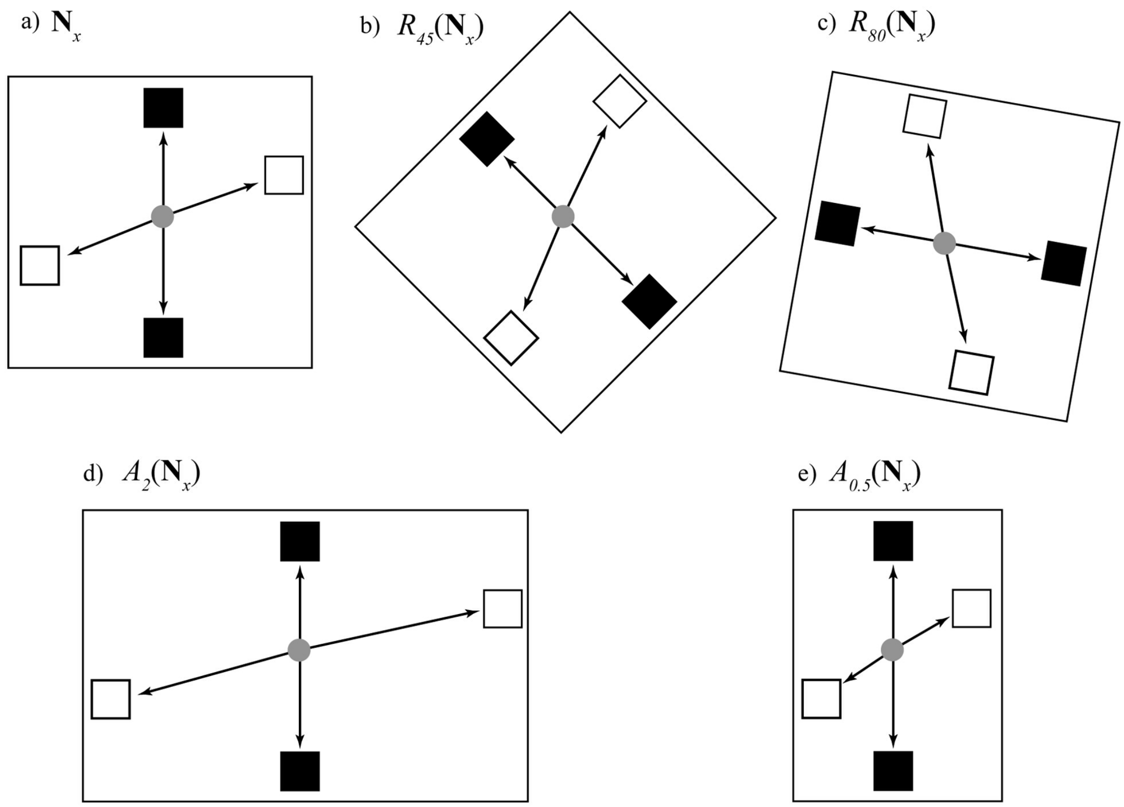

Figure 3. Different transformation applied to N_x. (a) Original neighborhood N_x. (b) Forty-five-degree rotation. (c) Eighty-degree rotation. (d) Factor 2 affinity along the *X* axis. (e) Factor 0.5 affinity along the *X* axis.

would be computationally unfeasible. It was often observed that training images contain certain idiosyncrasies that are not repetitive enough and therefore appear unchanged in the simulations. A good example is the "islands" in the classical channels training image in the work of *Strebelle* [2002]. In several cases one can find simulations where these islands are reproduced almost identically as in the training image. This lack of variability cannot appear with our method because the transform-invariant distances produce a large number of patterns from a single idiosyncrasy, therefore increasing the robustness of the multiple-point statistics.

[20] The distance in equation (3) could in theory be used with all simulation algorithms that rely on a distance between patterns, such as Simpat [*Arpat and Caers*, 2007], Filtersim [*Zhang et al.*, 2006], or Dispat [*Honarkhah and Caers*, 2010]. In particular, the Dispat method would be very well suited for this purpose since it also uses a distance to expand the space of the patterns that exist in the training image. However, these methods store all the patterns used for the simulation, and the increased pattern diversity brought by transform-invariant distances may lead to significant memory requirements and potential computational issues. In comparison, direct sampling does not have any storage constraints.

3.2. Transform-Invariant Distances Put in Practice

[21] To illustrate the method, we use the simplest possible training image that consists of a binary variable depicting parallel horizontal lines. This training image is simplistic, but represents a geologically meaningful spatial continuity. Concepts such as global connectivity or disconnectivity can be conveyed even at the scale of an elementary training image, which is much smaller than the simulation domain. We illustrate this by producing various spatial patterns with different transform-invariant distances. The elementary training image is displayed in Figure 4a, and realizations corresponding to different transformation parameters are shown in Figure 4b–4j. For all realizations in Figure 4, the direct sampling method was used with a distance threshold set to 0 and a neighborhood consisting of the closest 25 neighbors. The size of the training image is 100×100 pixels and the realizations are 500×500 pixels. Note that using such a small training image does not adhere to the general principle that recommends using a training image larger than the simulations. Using a larger version of this training image with standard multiple-point methods would not enrich the available patterns because those are repetitive. However, the realizations of Figure 4 show that using transform-invariant distances greatly increases the diversity of patterns.

[22] Figure 4b shows a realization that does not use transformations (i.e., rotations of 0° and an affinity factor of 1). It corresponds to what one would expect from a traditional multiple-point simulation method, with parallel lines that are sometimes disconnected because the training image does not inform the large-scale connectivity. Figure 4c is identical, except that a deterministic rotation of 45° is uniformly applied to all of the patterns. The result is similar to

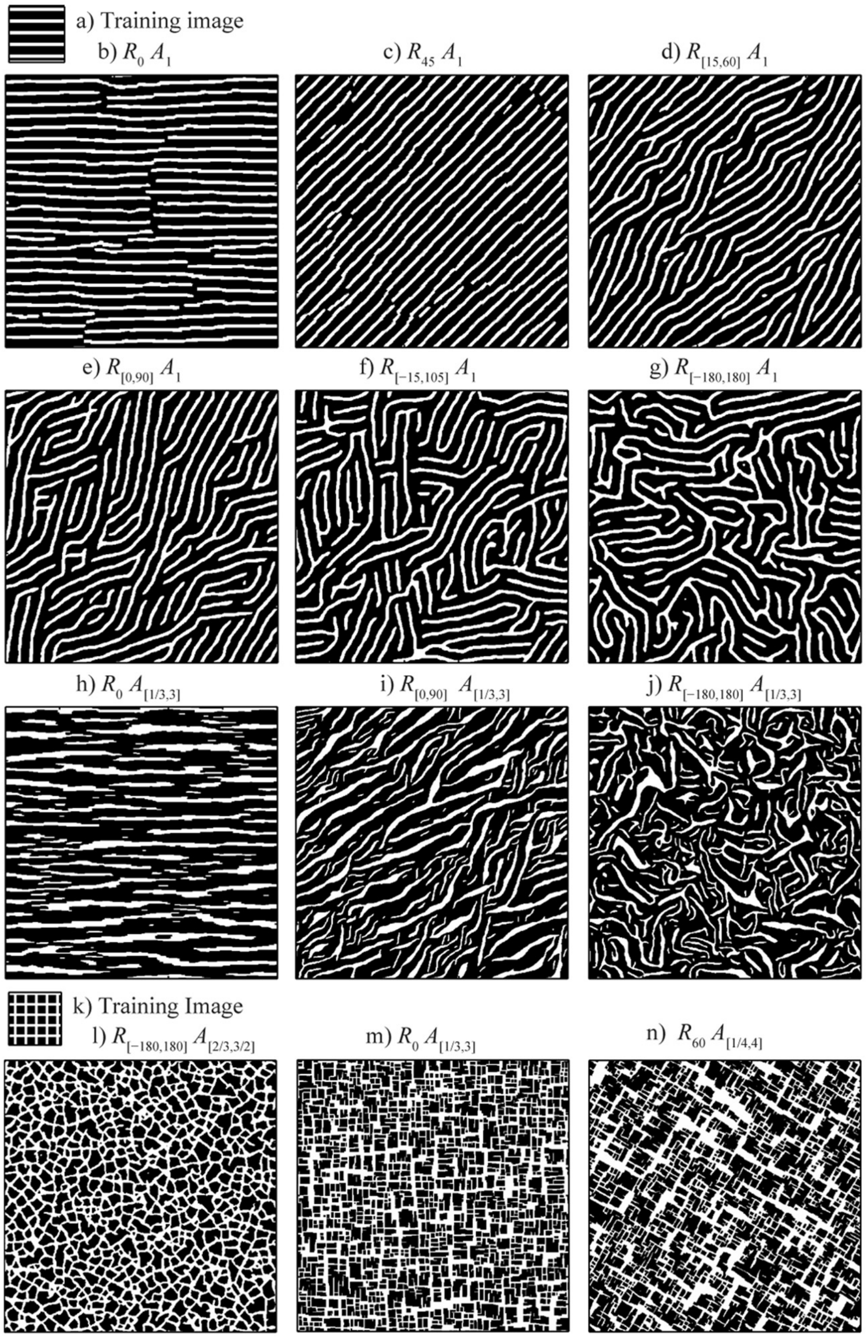

Figure 4. Examples of textures obtained with transform-invariant distances. (a) Lines training image. (b–j) Corresponding realizations with various transformation parameters. (k) Checkerboard training image. (l–n) Corresponding realizations with various transformation parameters. See the text for a detailed discussion.

that obtained with the transformations method proposed by *Strebelle and Zhang* [2004]. Unlike our approach, this method does not allow for an increase in the number of patterns available for simulation, neither does it allow for accounting the uncertainty in the transformation parameters. Additionally, it increases the computational load by creating as many data event catalogues as the number of categories of transformation parameters.

[23] Figure 4d is different because here the rotations are randomly distributed between 15° and 60°. The transform-invariant distance allows assembling patterns that respect the general continuity of the training image, even if those patterns are not oriented in the same direction. In Figure 4d, this produces coherent lines, but with a small degree of sinuosity. Since the patterns of the training image are reproduced up to a rotation, the pool of acceptable patterns is larger, resulting in increased continuity of the simulated lines. The diversity of patterns is not contained in the training image itself, but in the large amounts of possible transformations. Note that the lines almost never intersect

because patterns of intersection do not appear in the training image. Figure 4e uses angles between 0° and 90°, and it is visible that the extreme orientations of the structures tend to be either horizontal or vertical. Figure 4f shows even more variability in the orientations, and Figure 4g, with angles between $-180°$ and 180° allows a total freedom for the orientations, resulting in maze-like structures. Figure 4h–4j include, in addition to rotations, random affinity transforms ranging between 1/3 and 3. When rotations and affinities are used simultaneously, the added diversity of patterns creates shapes that can resemble geological structures such as clay drapes seen in cross-section (Figure 4h) or anastomosed channels seen in plan view (Figure 4i).

[24] In these examples, the training image only carries a concept of "elongated and connected bodies" that can materialize in various ways under the different transformations applied. Another case with a different training image is also represented in Figure 4k–4n. Figure 4k shows a training image carrying a concept corresponding to "disconnected bodies separated by interconnected interfaces." Using random rotations between $-180°$ and 180°, it is possible to obtain structures resembling desiccation cracks or, if applied in 3-D, certain types of porous media (Figure 4l). With random affinity transforms, the results tend to look like fractured or karstic media observed in areas with orthogonal stress fields or regions of overburden stress relief (Figure 4m and 4n). Note that this exercise could be continued using different elementary training images and transformation parameters to generate various families of structures corresponding to the cases presented in Figure 1.

[25] Although the transformations are randomly applied, spatial coherence is preserved throughout all of the examples. This is possible because the transformation parameters at each location are determined on the fly when simulating each value $Z(\mathbf{x})$. For each node, the formulation of equation (3) implies that the only acceptable transformations are the ones that yield patterns compatible with the training image. Therefore, it is ensured that the local transformations are consistent with the prescribed geological continuity. If the transformations were determined in advance, for example, using a map with an assigned rotation value at each location, the compatibility between the transformation parameters and the training image patterns would not be guaranteed.

4. Data-Driven Transformations

[26] A traditional conceptualization of geostatistics is that the spatial model is first derived from data, and then used for estimation or simulation. On the other hand, multiple-point simulation considers cases where the local data alone are not sufficient to infer a spatial model. However, conditioning point data, especially if present in large amounts, can influence the simulated structures and hence the underlying random function.

[27] As noted by *Mariethoz and Renard* [2010] one can distinguish two kinds of constraints that apply to determining the value of each pixel: the structural constraints and the local constraints. Structural constraints are imposed by the spatial model, which in this case consists of patterns of the training image, considered up to a transformation. Local constraints are given by conditioning point data. To obtain consistent simulations, these two types of constraints must be compatible. An example of incompatibility is the use of conditioning data showing continuity along the X axis with a training image that depicts channels running along the Y axis.

[28] When using transform-invariant-distances, the structural model is flexible and can adapt itself to the conditioning data. The minimization argument in equation (3) means that the transformation parameters are always adapted to maximize compatibility with the neighboring pixels, with respect to both structural and local constraints. Therefore, when conditioning point data are present, the issue of incompatibility between training image patterns and conditioning data is not as acute as with the classical approach. The patterns are automatically adapted to obtain as much compatibility as possible, and the final result is that the simulated structures are seamlessly wrapping around the data without user intervention.

[29] A practical example would be when integrating interpreted structural surfaces in a geological model (which could have been derived from a geophysical survey, for example, a seismic profile). This information is often characterized by a series of points along known interfaces (Figure 5a). The subsurface models should present structures globally oriented along the delineated interfaces, but showing some variability away from these known interfaces. This problem is easily dealt with using rotation-invariant distances and an elementary training image (here we use the lines training image shown in Figure 5b). Even if the data show relatively complex orientations, the patterns within the training image are oriented to maximize the coherence with the conditioning point data. As a consequence, the realizations (Figure 5c) respect the structures within the training image (structural constraints), but with orientations that are compatible with the data (local constraints). The distance threshold is set to 0 and the number of neighbors to 25. Figure 5d shows the probability of occurrence of the white facies (conductive layers) computed after 100 realizations. In the vicinity of the delineated interfaces, strong local constraints result in very well-defined orientations, with a series of three or four parallel layers that are present in most realizations. Away from the data, less local constraints are present and more variability between realizations is observed in the orientation of the layers.

5. Using Nonstationary Transformation Parameters for Structural Modeling

[30] Nonstationarity is often defined as a parametric trend in the values of the variable considered (e.g., a polynomial function). Such trends can be modeled in a variety of ways [see *Goovaerts*, 1997]. On the other hand, structural nonstationarity (such as a transition from channels to lobes) is usually too complex to be modeled with a few parameters and needs to be defined in a nonparametric way. Several authors have proposed methods of modeling nonstationarity in the context of multiple-point simulation [*Chugunova and Hu*, 2006; *De Vries et al.*, 2009; *Straubhaar et al.*, 2011], but these methods require either very complex training images that are difficult to obtain, or a very precise zonation of the domain that can be quite cumbersome in practice.

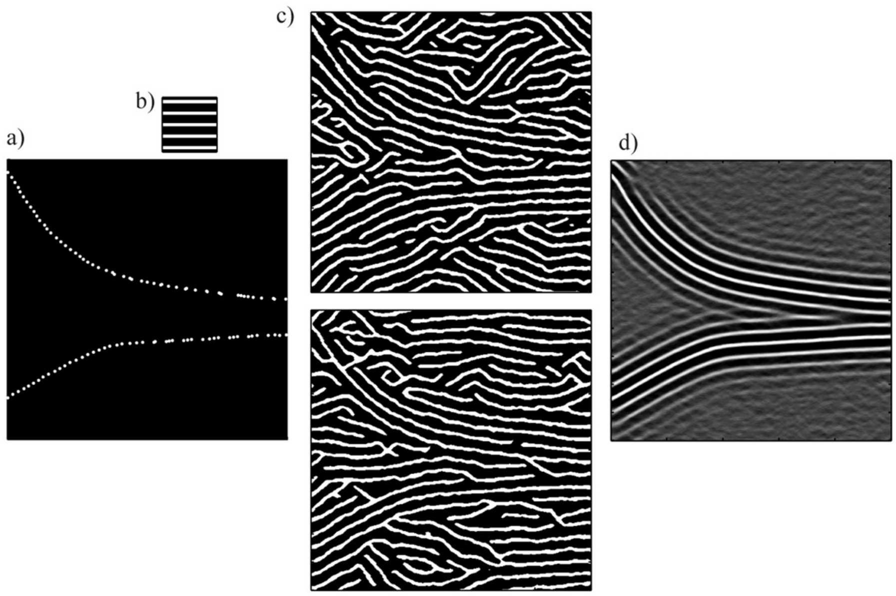

Figure 5. Illustration of the integration of interfaces derived from seismic profiles. (a) Pointed locations along interfaces (derived from seismic profile). (b) Elementary training image. (c) Two different data-driven realizations. (d) Probability of conductive layer (white) computed using 100 realizations.

[31] The examples shown in Figure 4 use homogeneous transformation parameters (i.e., identical bounds for transformation parameters are applied at all locations of the domain). In this section we propose to model structural nonstationarity simply by imposing nonstationary transformation parameters on the simulation domain.

5.1. Modeling Structural Folding With Rotation Operations

[32] The focus of this section is to consider variable transformation parameters to model nonstationary geological structures, especially the ones involving rotations such as folds. Such geological modeling is usually accomplished using geomodeling techniques [*Mallet*, 2008]. Among these, the implicit approach, based on level set methods, has received a lot of interest in the last few years [*Lajaunie et al.*, 1997; *Maxelon and Mancktelow*, 2005; *Maxelon et al.*, 2009]. Its main principle is to define 3-D scalar fields (or potential fields) whose isosurfaces are the geological interfaces. The potential fields are obtained by interpolation of local facies and orientation data. While facies measurements give the value of the potential at specific locations, orientation data provide information on the gradient of the potential field, and can thus be used to guide the interpolation. One advantage of these approaches is that they allow one to model a set of surfaces accounting for all orientation data with a single interpolation. In fact, a 3-D model can be built using only the simplest field measurements taken by geologists consisting of facies and orientation data, namely strike and dip measurements. In this section we show how our approach can be used as an alternative for obtaining 3-D models based on similar field measurements.

[33] Let us consider M angle measurements m_i, $i = 1 \ldots M$. For simplicity, we only consider the dip angle (i.e., the angle between the horizontal plane and the inclined surface), but the approach is general and can be applied to strike and dip together. Interpolation is needed in order to obtain the transformation parameters (orientations) on the entire domain. To this end, we will see that it is more convenient to express the bounds $[a,b]$ for the rotations as a median value $\alpha(\mathbf{x})$ and a tolerance $\varepsilon(\mathbf{x})$. For example, using $\alpha = 30$ and $\varepsilon = 10$ is equivalent to using the bounds [20,40].

[34] At the location $\mathbf{x}_i$ of an orientation measurement, assuming no measurement error, one can safely define $\alpha(\mathbf{x}_i) = m_i$ and $\varepsilon(\mathbf{x}_i) = 0$. This is equivalent to using infinitely narrow bounds in the transformation parameters: $[a,b] = [m_i,m_i]$. At locations further away from the measurement, the bounds defining the orientation should be enlarged and become $[a,b] = [\alpha(\mathbf{x}) - \varepsilon(\mathbf{x}), \alpha(\mathbf{x}) + \varepsilon(\mathbf{x})]$. We propose the use of simple interpolation techniques to obtain the transformation parameters $\alpha(\mathbf{x})$ and $\varepsilon(\mathbf{x})$ on the entire simulation domain. The most logical choice would be to use kriging for this interpolation. A major advantage would then be that the tolerance ε could be directly related to the estimation variance. The final result would provide an estimation of the angle and the tolerance on the entire domain that would be consistent with the field measurements. Unfortunately, in most practical cases the orientations are nonstationary and the measurements too few to properly compute and adjust a variogram. Hence, we propose a simple inverse square distance interpolation of the angles. The interpolated angles are then

$$\alpha(\mathbf{x}) = \sum_i \frac{w_i(\mathbf{x})\alpha_i}{\sum_j w_j(\mathbf{x})}, \quad w_i = \frac{1}{\|\mathbf{x} - \mathbf{x}_i\|^2}. \tag{4}$$

[35] Note that the angles actually represent a continuum with the highest values being similar to the lowest. For example, angles of 175° and −175° are only 10° apart, hence particular care has to be taken to avoid considering them as 350° apart. To take account for this, we use an

intermediate step proposed by *Gumiaux et al.* [2003], which addresses the issue by separately interpolating the sine and the cosine of α. Here we use equation (4) for this interpolation step. Reconstruction of $\alpha(\mathbf{x})$ is then done over the entire domain using its sine and cosine values.

[36] The tolerance is defined in an ad hoc way by considering the ratio between the distance to the closest data location and the domain size S, and multiplying it by a maximum tolerance $\varepsilon_{\max}$:

$$\varepsilon(\mathbf{x}) = \frac{\arg\min(\|\mathbf{x} - \mathbf{x}_i\|)}{S}\varepsilon_{\max}. \quad (5)$$

[37] The goal is to have $\varepsilon(\mathbf{x}) = 0$ at the orientation measurement locations and a maximum tolerance of $\varepsilon_{\max}$ (i.e., the highest uncertainty) at the locations that are the furthest away from the measurements. We use such basic interpolation of the rotation parameters because we consider cases where only a handful of orientation measurements are available. A variety of angle interpolation techniques could be used for this. For a comprehensive review of interpolation methods applied to angles the reader can refer to *Gumiaux et al.* [2003]. Once $\alpha(\mathbf{x})$ and $\varepsilon(\mathbf{x})$ are known over the entire simulation domain, realizations can be generated as previously with distance (1), the only difference being that the transformation parameters are spatially variable.

[38] Figure 6 illustrates the proposed methodology. Three orientation measurements are displayed by vectors on Figure 6a. Figure 6b and 6c represent, respectively, the result of the interpolated angles (in degrees) using equation (4), and the tolerance obtained using equation (5) with a maximum tolerance $\varepsilon_{\max}$ of 90°.

[39] For the simulation, two different training images are considered (Figure 6d). The first one is continuous and represents hydraulic conductivity. It consists of one unconditional multi-Gaussian realization of 200 × 200 pixels generated by the spectral method [*Le Ravalec-Dupin et al.*, 2000]. An exponential variogram model is used with a mean of −4 and a variance of 2. A strong anisotropy is represented by ranges of 120 in the X direction and 5 in the Y direction. The second training image, consisting of horizontal lines representing hydrofacies, is the same as in Figure 4a. One realization is generated with each training image. The distance threshold is set to 0 for the categorical simulation, 0.02 for the continuous simulation, and the number of neighbors is set to 25 in both cases. These two realizations are shown in Figure 6e and 6f. For both training images, the structures of the training image are oriented in a way that is consistent with the initial measured orientations $m(\mathbf{x}_i)$. Moreover, the continuities are well preserved, with elongated bodies of high hydraulic conductivity in the continuous case and parallel channels of constant thickness in the categorical case.

[40] To investigate the sensitivity of the maximum tolerance $\varepsilon_{\max}$, we perform exactly the same exercise with $\varepsilon_{\max} = 180°$. As a result, the interpolated angles remain the same but all tolerance values are doubled compared to Figure 6c, globally increasing the variability of orientations. The resulting simulations, shown in Figure 7, indeed present more erratic channel orientations while being consistent at the measurement locations.

[41] To compare the channel orientations over an ensemble of realizations, we perform a skeleton analysis of 100 categorical realizations with (1) $\varepsilon_{\max} = 90°$ and (2) $\varepsilon_{\max} = 180°$. Skeleton analysis is a morphological operation that involves removing pixels on the boundaries of objects, but not allowing the objects to break apart. As a result, each channel is represented by a line that runs through its center. The results are shown in Figure 8. Note that in order to keep Figure 8 readable, we simultaneously

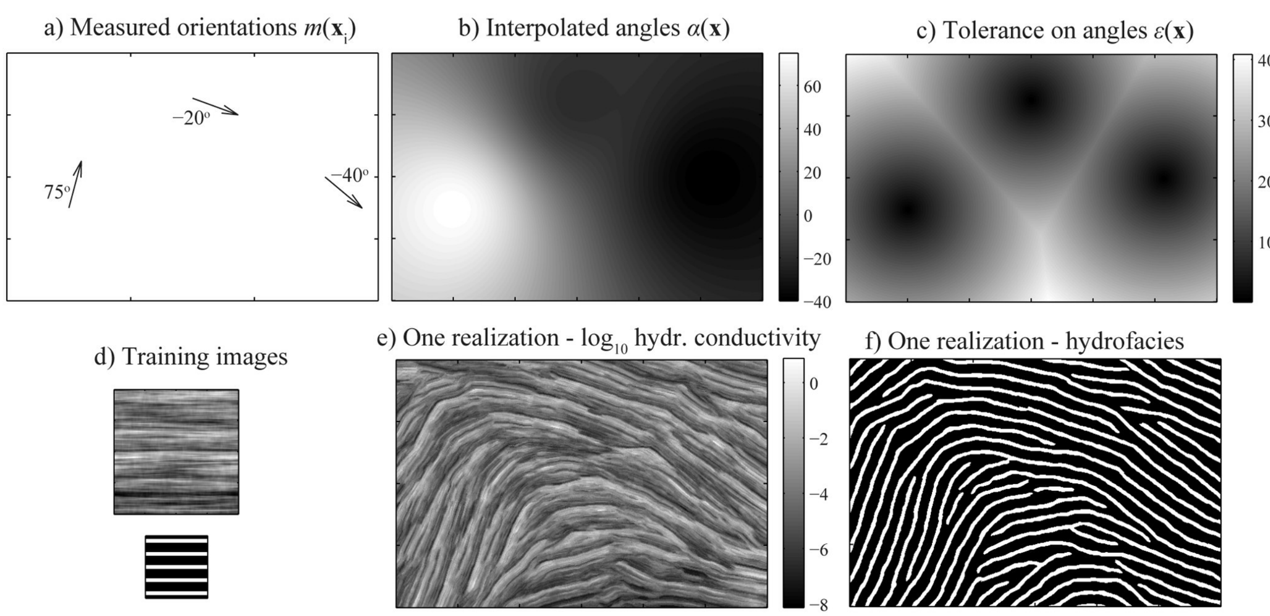

Figure 6. Application of nonstationary transformation parameters to model a fold in 2-D, with $\varepsilon_{\max} = 90°$. (a) Orientation measurements. (b and c) Interpolated rotation parameters. (d) Two different training images. (e and f) Corresponding realizations.

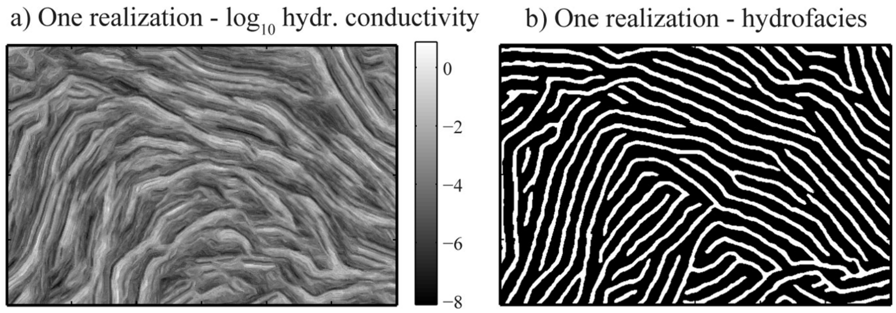

Figure 7. Identical example with a value of $\varepsilon_{\max} = 180°$. (a) Continuous variable. (b) Categorical variable.

represent the skeleton analysis of only five realizations in each case. In both cases, the channels are all correctly oriented at the data locations (thus, resulting in parallel lines), but they can represent a large amount of variability at locations distant from the data, such as the lower central portion or the top left corner of the image, where the lines cross each other, showing different orientations from one realization to the next. The orientation variability is much lower in Figure 8a than in 8b due to the lower $\varepsilon_{\max}$ value that controls the tolerance on angles. However, within a single realization the channels remain relatively parallel to each other, as shown in Figure 7b, due to the parallel structures found in the training image.

[42] Increasing the number of orientation measurements allows obtaining geological structures of increasing complexity. Figure 9 illustrates a situation with eight orientation measurements, with the same training images as used in Figure 6. The interpolated angles result in a succession of two different folds. Figure 10 shows an example where even more complexity has been introduced using distances that are both rotation- and affinity-invariant. In addition to the rotation and tolerances shown in Figure 10b and 10c, we include random affinity transforms ranging uniformly between 1/3 and 3 on the entire domain. The resulting structures have variable widths and are not parallel any more, corresponding to sedimentary structures observed in deltaic environments. Note that both examples of Figures 9 and 10 use a value of $\varepsilon_{\max} = 90°$.

5.2. High-Resolution 3-D Example

[43] Within the framework of classical multiple-point simulation, finding a complex training image representing all desired structures can be difficult in 2-D. In 3-D, the problem becomes even more acute. Nonstationarity may require using a training image of increased complexity or even multiple training images. In fact, in order to build a consistent 3-D training image, it can be necessary to perform a full geomodeling exercise, using either other stochastic simulation methods, e.g., Boolean [*Boucher et al.*, 2010; *Comunian et al.*, 2011; *Maharaja*, 2008] or pluri-Gaussian], or specific algorithms contained in commercial geomodeling packages. An advantage of the Boolean method is that it is possible to parameterize each facies separately, whereas our method transforms entire data events, regardless of which facies are affected. On the other hand, object-based training images have important drawbacks, such as the necessity to deal with categorical variables, and the high computational costs incurred by large and complex training images. In 2-D, it is possible to use analogues as training images, but the analog may not present the appropriate properties of stationarity and size relative to the richness of patterns. In comparison, our approach is simpler.

[44] To demonstrate the value and the practicality of our methodology, we present a 3-D synthetic aquifer modeled with elementary 3-D training images and rotation-invariant distances. Six orientation measurements are available

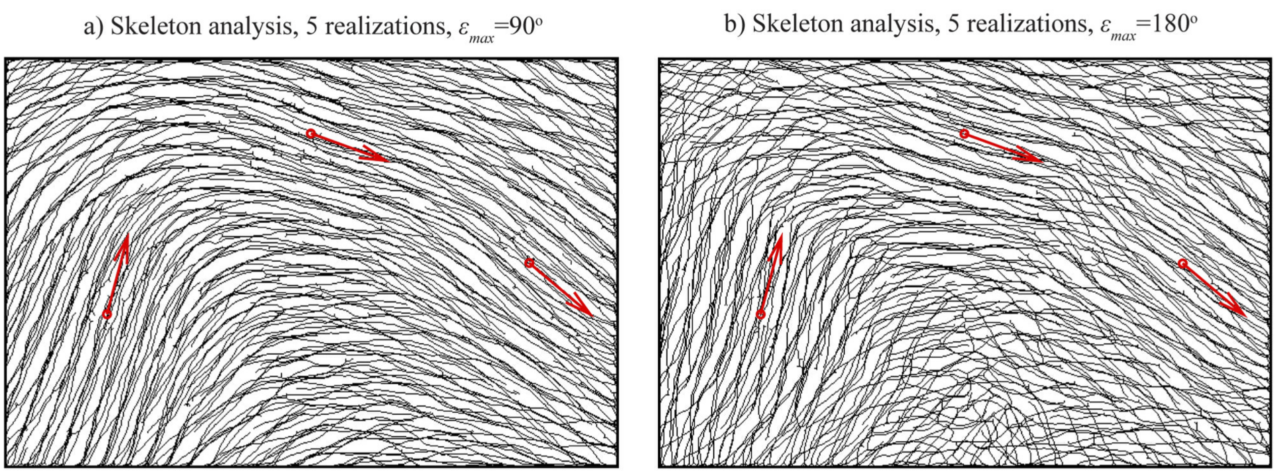

Figure 8. Skeleton analysis of realizations obtained with (a) $\varepsilon_{\max} = 90°$ and (b) $\varepsilon_{\max} = 180°$.

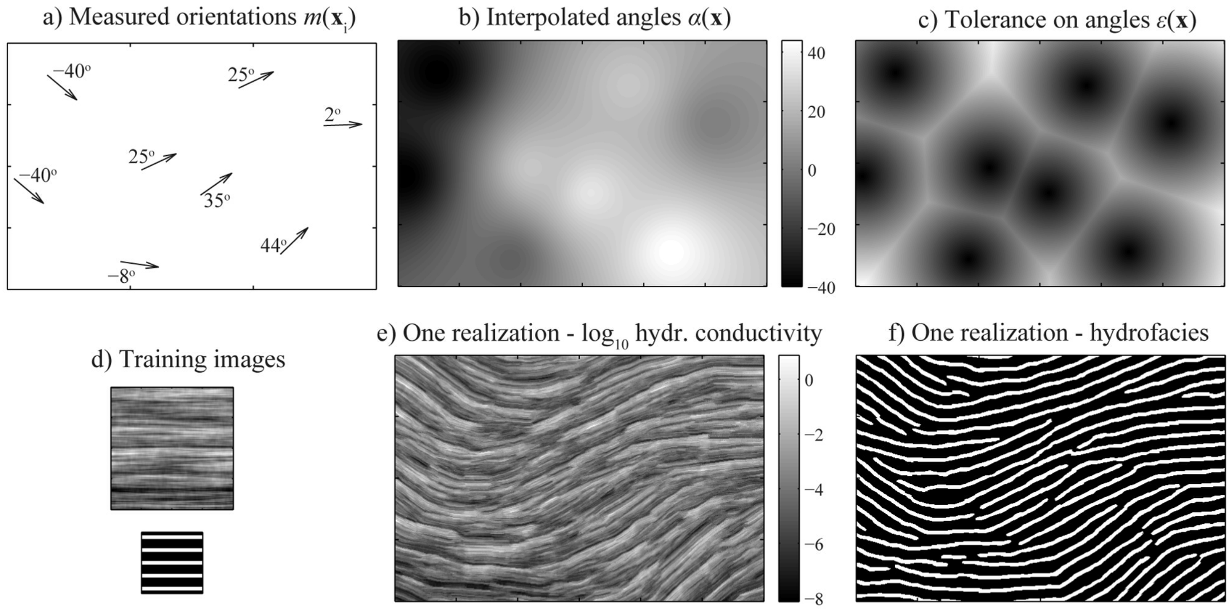

Figure 9. Application of nonstationary transformation parameters to model a double fold in 2-D. (a) Orientation measurements. (b and c) Interpolated rotation parameters. (d) Two different training images. (e and f) Corresponding realizations.

(Figure 11a), which correspond to a relatively complex geological structure consisting of an anticline on one side of the domain and a syncline on the other side. As for the previous examples, we perform simulations for both categorical and continuous cases using two different training images.

[45] The categorical training image (Figure 11b) is binary and made of horizontal equally spaced layers. The continuous training image (Figure 11c) represents $\log_{10}$ hydraulic conductivity. It has the same structure as the categorical one, with each category populated using an unconditional multi-Gaussian realization generated by the spectral method. For both facies, exponential variograms are used with ranges of 100 units in the X and Y directions and five units in the Z direction. For the regions corresponding to facies 0 (transparent on the figures), a mean $\log_{10}$ hydraulic conductivity of -6 is used. For facies 1 the mean $\log_{10}$ hydraulic conductivity is set to -3. For both facies a variance of 2 was chosen. Both categorical and

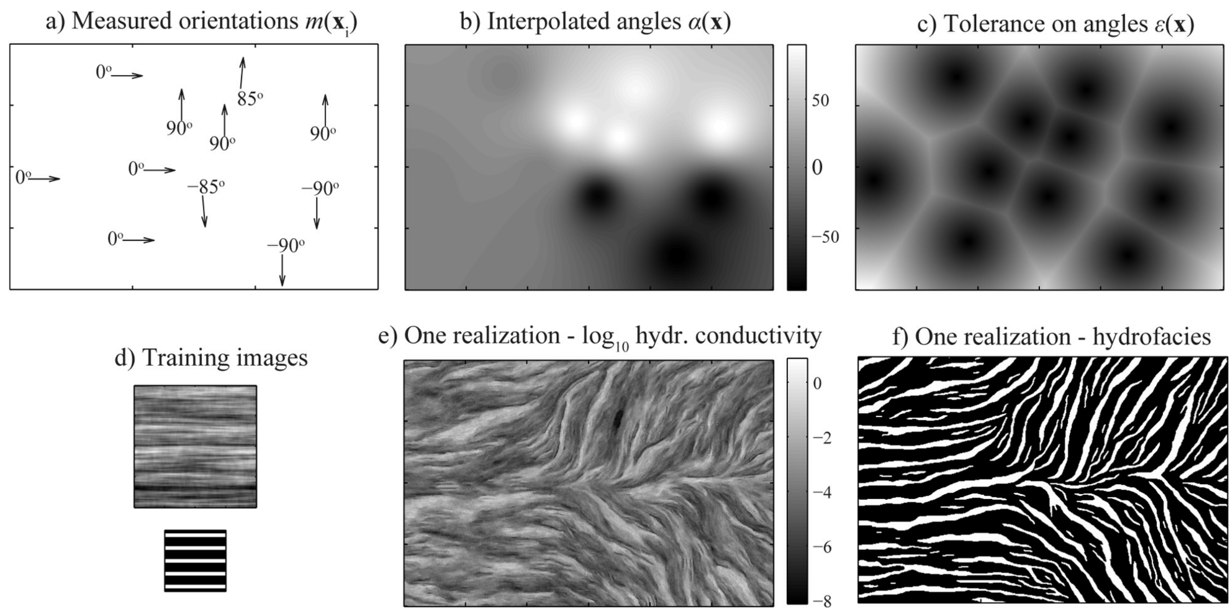

Figure 10. Application of nonstationary transformation parameters to model deltaic structures in 2-D. (a) Orientation measurements. (b and c) Interpolated rotation parameters. In addition, uniform affinity-invariant transforms are used corresponding to $A_{[1/3,3]}$. (d) Two different training images. (e and f) Corresponding realizations.

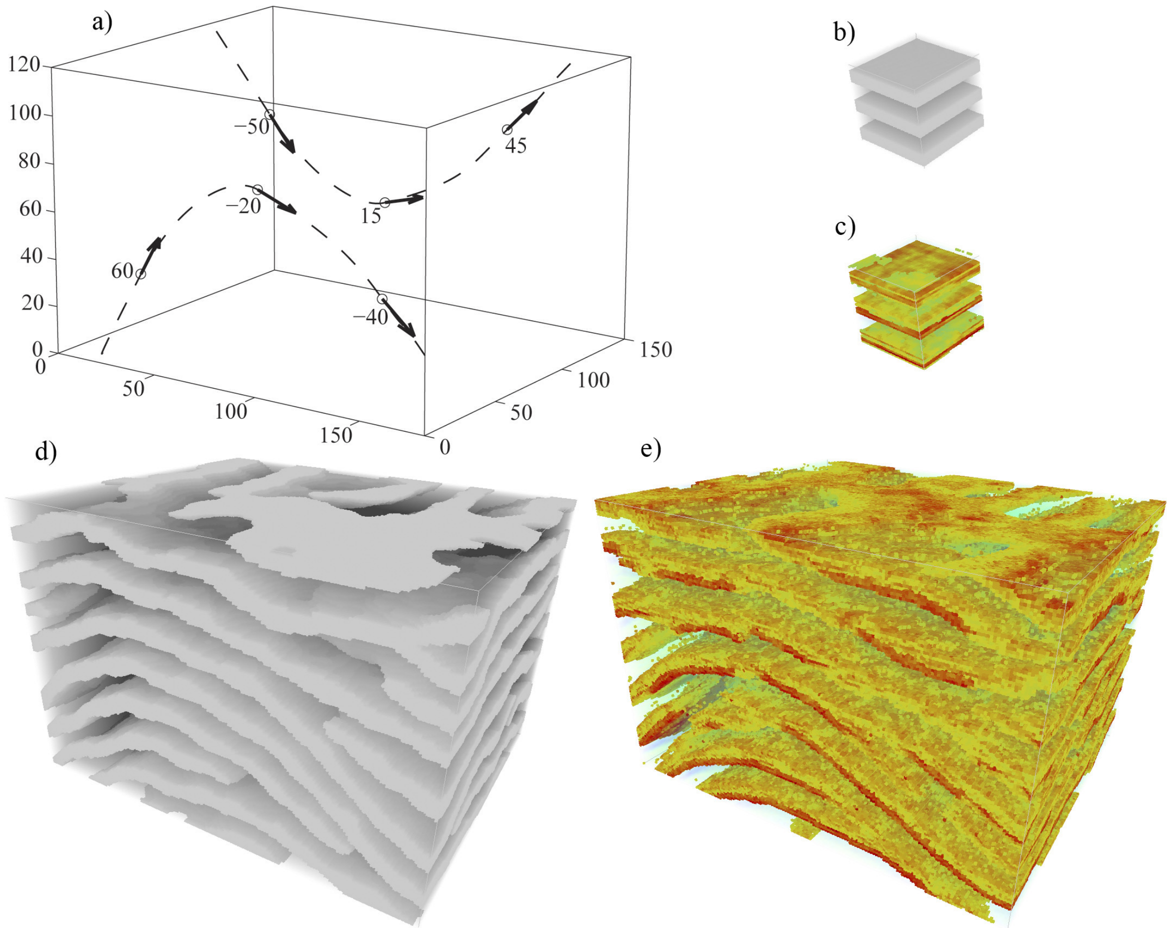

Figure 11. A high-resolution 3-D example of the use of elementary training images with transform-invariant distances. (a) Six orientation data depicting an anticline on one side of the domain and a syncline of the other side. (b and c) Elementary training images. (d and e) Corresponding realizations.

continuous training image sizes are 40 × 40 × 40 grid nodes, which is small compared to the simulation domain that measures 180 × 150 × 120 grid nodes.

[46] Interpolation of the angles in 3-D is performed using equation (4). The angle tolerances are defined using equation (5), with $\varepsilon_{\max} = 90°$. In the direct sampling simulation, the distance threshold is set to 0.1 for the categorical simulation, 0.03 for the continuous simulation, and the number of neighbors is 25 for both cases. Figure 11d and 11e show the resulting realizations for both categorical and continuous cases. Note that the computation times are kept reasonable because of the small size of the training image. For the categorical case, the simulation of 3.24 million grid nodes takes about 1 h on a dual core 2.5 Ghz laptop, using the parallelization approach described in *Mariethoz* [2010] to take advantage of the computation capacity of both CPUs. Note that this result is obtained by using a relatively high distance threshold (0.1), producing simulations with satisfying large-scale structures, but that are noisy at a small scale. In a second step, the noise is removed by resimulating all pixels with a reduced neighborhood.

[47] This example demonstrates that it is suitable to use elementary training images in complex geological environments where the classical multiple-point approach would be difficult to put into practice. Our methodology is not intended to replace structural grid transformation methods [e.g., *Caers*, 2005; *Mallet*, 2008]. However, it can be an interesting alternative for modeling structural uncertainty in cases where, although the general structures are known, one wants several alternative realizations of a structural model. This situation corresponds to the setting of the examples depicted in Figures 8 and 11.

6. Discussion and Conclusion

[48] We present a new framework for multiple-point simulation involving the use of elementary training images and transform-invariant distances. Transformations (rotations and/or affinity in the cases presented) are randomly applied to the patterns of the training image resulting in a vast family of geological structures that all display a type of geological continuity related to the training image. The transform-invariant distances are chosen with the goal of reproducing specific characteristics of the training image, such as connectivity patterns that have a strong impact on flow and transport, while leaving a degree of freedom in other characteristics such as the orientation or the anisotropy of the structures. Note that other transformations could be used, such as symmetries or shifts. The advantages of this method are that the training images are so

simple that they can be easily built, even in 3-D. After the random transformations have been applied, complex geological structures are obtained, whose spatial structures can be parameterized by adjusting the statistics of the random transformations, based on field data or geological context. Overall, our methodology is a simple way of shaping the prior spatial model, which is possible in most cases by adjusting two numbers only.

[49] We apply the method on a synthetic example involving seismic data where the transformation parameters are data-driven. We also show examples where realistic 2-D and 3-D structures are built from simplistic training images, with transformation parameters inferred using a small number of data. In the 3-D case, our method can also be used in a similar way as geomodeling tools using the implicit approach. In fact, it requires the same type of data, consisting of facies and orientation measurements.

[50] The simple parameterization of complex geological structures can be very useful in the context of inverse problems where the prior model of spatial continuity is uncertain. The transformation parameters could be inferred either with an inverse procedure or by direct adjustment to the data, as is currently done with variograms. Although these topics are not the focus of this paper, we see them as important future research areas.

[51] Another possible direction for future research would be to adapt the concept of transform-invariant distances to pattern-based simulation algorithms. The main challenge would be computational issues related to the storage requirements of the numerous transformed patterns.

[52] One fundamental issue raised by the use of elementary training images is that the training image is no longer a direct reflection of the structures deemed to exist in the subsurface, but rather a vehicle for geological representation. In fact, multiple-point simulation is often seen as a process which, given a training image, produces other images (simulations) with identical statistical properties and possibly anchored to conditioning data. However, it has been noted [*Boucher*, 2007; *Journel and Zhang*, 2006] that one cannot expect a complete statistical similarity between the training image and the corresponding simulations. In fact, the algorithmic machine lies between the training image and the simulation results. The function that produces a simulation is algorithmicallydefined, and hence intractable. With the same training image, different implementations of a multiple-point simulation algorithm can produce different simulation results. Each algorithm is implemented in a specific way and takes different parameters that may not have their counterpart in other implementations. In this context, a viable way of validating a training image and the associated parameters is to perform an a posteriori check to investigate whether the simulated structures correspond to what is expected by the geologist. In practice, this geological validation is largely used for both MPS and covariance-based simulation methods. More formal ways would call for inferring the training image based on field measurements, through inversion or cross-validation. This is an active and promising research topic.

[53] In this paper we acknowledge that the training image is only an initial representation of the subsurface which is further processed by the simulation algorithm. Hence, we propose an alternative paradigm where the training image represents broad spatial concepts rather than a specific geological reality. The training images used are very simple, and complexity emerges from random transformations that are guided by conditioning data or by local orientations.

[54] **Acknowledgments.** This work was supported by the Australian Research Council, the National Water Commission, and the Swiss National Science Foundation (grant PBNEP2-124334). We thank Andre Journel, David Ginsbourger, Sanjay Srinivasan, and Juan Fernández-Martinez for fruitful brainstorming sessions and Philippe Renard, Julien Straubhaar, Jef Caers, and two anonymous reviewers for their constructive comments.

References

Allard, D., R. Froidevaux, and P. Biver (2006), Conditional simulation of multi-type non stationary Markov object models respecting specified proportions, *Math. Geosci.*, *38*(8), 959–986, doi:10.1007/s11004-006-9057-5.

Arpat, B., and J. Caers (2007), Conditional simulations with patterns, *Math. Geol.*, *39*(2), 177–203.

Bárdossy, A., and J. Li (2008), Geostatistical interpolation using copulas, *Water Resour. Res.*, *44*, W07412, doi:10.1029/2007WR006115.

Bastante, F., C. Ordóñez, J. Taboada, and J. Matías (2008), Comparison of indicator kriging, conditional indicator simulation and multiple-point statistics used to model slate deposits, *Eng. Geol.*, *98*(1–2), 50–59, doi:10.1016/j.enggeo.2008.01.006.

Boucher, A. (2007), Algorithm-driven and representation-driven random function: A new formalism for applied geostatistics, edited, Stanford Center for Reservoir Forecasting, Stanford, CA.

Boucher, A., R. Gupta, J. Caers, and A. Satija (2010), Tetris: A training image generator for SGeMS, paper presented at Proceedings of 23nd SCRF annual affiliates meeting, Stanford University, May 5–6 2010.

Caers, J. (2003), History matching under a training image-based geological model constraint, *SPE J.*, *8*(3), 218–226, SPE # 74716.

Caers, J. (2005), *Petroleum Geostatistics*, 88 pp., Society of Petroleum Engineers, Richardson, TX.

Chugunova, T., and L. Hu (2006), Multiple-Point Statistical Simulaitons Constrained by continuous Auxiliary Data, paper presented at Int. Assoc. for Math. Geol. XIth International Congress, Université de Liège, Belgium.

Cojan, I., O. Fouche, S. Lopez, and J. Rivoirard (2004), Process-based reservoir modelling in the example of meandering channel, in *Geostatistics Banff*, edited by O. Leuangthong and C. Deutch, pp. 611–619, Springer, Berlin, Germany.

Comunian, A., P. Renard, J. Straubhaar, and P. Bayer (2011), Three-dimensional high resolution fluvio-glacial aquifer analog: Part 2: geostatistical modeling, *J. Hydrol.*, doi:10.1016/j.hydrol.2011.03.037, in press.

de Almeida, J. (2010), Stochastic simulation methods for characterization of lithoclasses in carbonate reservoirs, *Earth Sci. Rev.*, *101*(3–4), 250–270.

Deutsch, C., and L. Wang (1996), Hierarchical object-based stochastic modeling of fluvial reservoirs, *Math. Geol.*, *28*(7), 857–880, doi:10.1007/BF02066005.

Deutsch, C., and T. Tran (2002), FLUVSIM: A program for object-based stochastic modeling of fluvial depositional systems, *Comput. Geosci.*, *28*(4), 525–535.

De Vries, L., J. Carrera, O. Falivene, O. Gratacos, and L. Slooten (2009), Application of multiple point geostatistics to non-stationary images, *Math. Geosci.*, *41*(1), 29–42.

Dimitrakopoulos, R., H. Mustapha, and E. Gloaguen (2010), High-order statistics of spatial random fields: Exploring spatial cumulants for modeling complex non-Gaussian and non-linear phenomena, *Math. Geosci.*, *42*(1), 65–99.

Efros, A., and T. Leung (1999), Texture synthesis by non-parametric sampling, paper presented at The Proceedings of the Seventh IEEE International Conference on Computer Vision, 1999, Kerkyra, Greece.

Emery, X. (2007), Using the Gibbs sampler for conditional simulation of Gaussian-based random fields, *Comput. Geosci.*, *33*(2007), 522–537.

Emery, X., and J. Ortiz (2011), A comparison of random field models beyond bivariate distributions, *Math. Geosci.*, *43*(2), 183–202, doi:10.1007/s11004-010-9305-6.

Feyen, L., and J. Caers (2006), Quantifying geological uncertainty for flow and transport modelling in multi-modal heterogeneous formations, *Adv. Water Resour.*, *29*(6), 912–929.

Gómez-Hernández, J. J., and X.-H. Wen (1998), To be or not to be multi-gaussian? A reflection on stochastic hydrogeology, *Adv. Water Resour.*, *21*(1), 47–61.
Gonzales, E., T. Mukerji, and G. Mavko (2008), Seismic inversion combining rock physics and multiple-point geostatistics, *Geophysics*, *73*(1), R11–R21, doi:10.1190/1.2803748.
Goovaerts, P. (1997), *Geostatistics for Natural Resources Evaluation*, Oxford University Press, Oxford, U. K.
Green, C., J. Böhlke, B. Bekins, and S. Philips (2010), Mixing effects on apparent reaction rates and isotope fractionation during denitrification in a heterogeneous aquifer, *Water Resour. Res.*, *46*, W08525, doi:10.1029/2009WR008903.
Gumiaux, C., D. Gapais, and J. Brun (2003), Geostatistics applied to best-fit interpolation of orientation data, *Tectonophysics*, *376*(3–4), 241–259.
Honarkhah, M., and J. Caers (2010), Stochastic simulation of patterns using distance-based pattern modeling, *Math. Geosci.*, *42*(5), 487–517, doi:10.1007/s11004-010-9276-7.
Hu, L., and T. Chugunova (2008), Multiple-point geostatistics for modeling subsurface heterogeneity: A comprehensive review, *Water Resour. Res.*, *44*, W11413, doi:10.1029/2008WR006993.
Huysmans, M., and A. Dassargues (2009), Application of multiple-point geostatistics on modelling groundwater flow and transport in a cross-bedded aquifer (Belgium), *Hydrogeol. J.*, *17*, 1901–1911.
Journel, A., and T. Zhang (2006), The necessity of a multiple-point prior model, *Math. Geol.*, *38*(5), 591–610.
Keogh, K., A. Martinius, and R. Osland (2007), The development of fluvial stochastic modelling in the Norwegian oil industry: A historical review, subsurface implementation and future directions, *Sediment. Geol.*, *202*(1–2), 249–268.
Kitanidis, P. (1995), Quasi-linear geostatistical theory for inversing, *Water Resour. Res.*, *31*(10), 2411–2419, doi:10.1029/95WR01945.
Klise, K., G. Weissmann, S. McKenna, E. Nichols, J. Frechette, T. Wawrzyniec, and V. Tidell (2009), Exploring solute transport and streamline connectivity using lidar-based outcrop images and geostatistical representations of heterogeneity, *Water Resour. Res.*, *45*, W05413, doi:10.1029/2008WR007500.
Knudby, C., and J. Carrera (2005), On the relationship between indicators of geostatistical, flow and transport connectivity, *Adv. Water Resour.*, *28*(4), 405–421.
Lajaunie, C., G. Courrioux, and L. Manuel (1997), Foliations field and 3D cartography in geology: Principles of a method based on potential interpolation, *Math. Geol.*, *29*(4), 571–584, doi:10.1007/BF02775087.
Lantuéjoul, C. (2002), *Geostatistical simulation: Models and Algorithms*, 232 pp., Springer, Berlin, Germany.
Le Loc'h, G., and A. G. Galli (1994), Improvement in the truncated Gaussian method: Combining several Gaussian functions, paper presented at Ecmor 4, 4th European Conference on the Mathematics of Oil Recovery, Roros, Norway, 7–10 June.
Le Ravalec-Dupin, M., B. Noetinger, and L. Y. Hu. (2000), The FFT moving average (FFT-MA) generator: An efficient numerical method for generating and conditioning Gaussian simulations, *Math. Geol.*, *32*(6), 701–723.
Lu, D., T. Zhang, J. Yamg, D. Li, and X. Kong (2009), A reconstruction method of porous media integrating soft data with hard data, *Chin. Sci. Bull.*, *54*(11), 1876–1885.
Maharaja, A. (2008), TiGenerator: Object-based training image generator, *Comput. Geosci.*, *34*(12).
Mallet, J.-L. (2008), *Numerical Earth Models*, EAGE Pub. BV, Houten, Netherlands.
Mariethoz, G. (2010), A general parallelization strategy for random path based geostatistical simulation methods, *Comput. Geosci.*, *37*(7), 953–958, doi:10.1016/j.cageo.2009.11.001.
Mariethoz, G., and P. Renard (2010), Reconstruction of incomplete data sets or images using Direct Sampling, *Math. Geosci.*, *42*(3), 245–268, doi:10.1007/s11004-010-9270-0.
Mariethoz, G., P. Renard, F. Cornaton, and O. Jaquet (2009), Truncated plurigaussian simulations to characterize aquifer heterogeneity, *Ground Water*, *47*(1), 13–24, doi:10.1111/j.1745-6584.2008.00489.x.
Mariethoz, G., P. Renard, and J. Straubhaar (2010), The direct sampling method to perform multiple-point simulations, *Water Resour. Res.*, *46*, W11536, doi:10.1029/2008WR007621.
Maxelon, M., and N. Mancktelow (2005), Three-dimensional geometry and tectonostratigraphy of the Pennine zone, Central Alps, Switzerland and Northern Italy, *Earth Sci. Rev.*, *71*(3–4), 171–227, doi:10.1016/j.earscirev.2005.01.003.
Maxelon, M., P. Renard, G. Courrioux, M. Brändli, and N. Mancktelow (2009), A workflow to facilitate three-dimensional geometrical modelling of complex poly-deformed geological units, *Comput. Geosci.*, *35*(3), 644–658, doi:10.1016/j.cageo.2008.06.005.
Michael, H., A. Boucher, T. Sun, J. Caers, and S. Gorelick (2010), Combining geologic-process models and geostatistics for conditional simulation of 3-D subsurface heterogeneity, *Water Resour. Res.*, *46*, W05527, doi:10.1029/2009WR008414.
Nowak, W., F. de Barros, and Y. Rubin (2010), Bayesian geostatistical design: Task-driven optimal site investigation when the geostatistical model is uncertain, *Water Resour. Res.*, *46*, W03535, doi:10.1029/2009WR008312.
Okabe, H., and M. Blunt (2007), Pore space reconstruction of vuggy carbonates using microtomography and multiple-point statistics, *Water Resour. Res.*, *43*, W12S02, doi:10.1029/2006WR005680.
Pyrcz, M., J. Boisvert, and C. V. Deutsch (2008), A library of training images for fluvial and deepwater reservoirs and associated code, *Comput. Geosci.*, *34*(5), 542–560.
Pyrcz, M., J. Boisvert, and C. Deutsch (2009), ALLUVSIM: A program for event-based stochastic modeling of fluvial depositional systems, *Comput. Geosci.*, *35*(8), 1671–1685, doi:10.1016/j.cageo.2008.09.012.
Ronayne, M., S. Gorelick, and J. Caers (2008), Identifying discrete geologic structures that produce anomalous hydraulic response: An inverse modeling approach, *Water Resour. Res.*, *44*, W08426, doi:10.1029/2007WR006635.
Sánchez-Vila, X., J. Carrera, and J. P. Girardi (1996), Scale effects in transmissivity, *J. Hydrol.*, *183*(1–2), 1–22.
Straubhaar, J., P. Renard, G. Mariethoz, R. Froidevaux, and O. Besson (2011), An improved parallel multiple-point algorithm using a list approach, *Math. Geosci.*, *43*(3), 305–328, doi:10.1007/s11004-011-9328-7.
Strebelle, S. (2002), Conditional simulation of complex geological structures using multiple-point statistics, *Math. Geol.*, *34*(1), 1–22.
Strebelle, S., and T. Zhang (2004), Non-stationary multiple-point geostatistical models, in *Geostatistics Banff*, edited by O. Leuangthong and C. Deutch, pp. 235–244, Springer, Berlin, Germany.
Suzuki, S., and J. Caers (2008), A distance-based prior model parameterization for constraining solutions of spatial inverse problems, *Math. Geosci.*, *40*(4), 445–469.
Western, A., G. Blöschl, and R. Grayson (2001), Toward capturing hydrologically significant connectivity in spatial patterns, *Water Resour. Res.*, *37*(1), 83–97, doi:10.1029/2000WR900241.
Wojcik, R., D. McLaughlin, A. Konings, and D. Entekhabi (2009), Conditioning stochastic rainfall replicates on remote sensing data, *IEEE Trans. Geosci. Remote Sens.*, *47*(8), 2436–2449.
Wu, J., A. Boucher, and T. Zhang (2008), A SGeMS code for pattern simulation of continuous and categorical variables: FILTERSIM, *Comput. Geosci.*, *34*(12), 1863–1876.
Zhang, T., P. Switzer, and A. Journel (2006), Filter-based classification of training image patterns for spatial simulation, *Math. Geol.*, *38*(1), 63–80.
Zinn, B., and C. F. Harvey (2003), When good statistical models of aquifer heterogeneity go bad: A comparison of flow, dispersion, and mass transfer in connected and multivariate Gaussian hydraulic conductivity fields, *Water Resour. Res.*, *39*(3), 1051, doi:10.1029/2001WR001146.

B. F. J. Kelly and G. Mariethoz, National Centre for Groundwater Research and Training, University of New South Wales, Anzac Parade, Sydney, NSW 2052, Australia. (gregoire.mariethoz@minds.ch)